Icarus 334 (2019) 11–21

Contents lists available at ScienceDirect

Icarus

journal homepage: www.elsevier.com/locate/icarus

The HST lightcurve of (486958) 2014 MU_{69}

S.D. Benecchi[a,*], S.B. Porter[b], M.W. Buie[b], A.M. Zangari[b], A.J. Verbiscer[c], K.S. Noll[d], S.A. Stern[b], J.R. Spencer[b], A.H. Parker[b]

[a] Planetary Science Institute, 1700 East Fort Lowell, Suite 106, Tucson, AZ 85719, United States of America
[b] Southwest Research Institute, 1050 Walnut St., Suite 300, Boulder, CO 80302, United States of America
[c] University of Virginia, Department of Astronomy, PO Box 400325, Charlottesville, VA 22904, United States of America
[d] NASA Goddard Space Flight Center, 8800 Greenbelt Rd. Code 693, Greenbelt, MD 20771, United States of America

ARTICLE INFO

Keywords:
Kuiper Belt
Photometry
Hubble space telescope observations
KBO
NASA missions

ABSTRACT

We report *Hubble Space Telescope* (HST) lightcurve observations of the *New Horizons* spacecraft encounter Kuiper Belt object (KBO) (486958) 2014 MU_{69} acquired near opposition in July 2017. In order to plan the optimum flyby sequence the *New Horizons* mission planners needed to learn as much as possible about the target in advance of the encounter. Specifically, from lightcurve data, encounter timing could be adjusted to accommodate a highly elongated, binary, or rapidly rotating target. HST astrometric (Porter et al., 2018) and stellar occultation (Buie et al., 2018) observations constrained MU69's orbit and diameter (21–41 km for an albedo of 0.15–0.04), respectively. Photometry from the astrometric dataset suggested a variability of ≥0.3 mags, but they did not determine the period or provide shape information. To that end we strategically spaced 24 HST orbits over 9 days to investigate rotation periods from approximately 2–100 h and to better constrain the lightcurve amplitude. Until *New Horizons* detected MU69 in its optical navigation images beginning in August 2018, this HST lightcurve campaign provided the most accurate photometry to date. The mean variation in our data is 0.15 magnitudes which suggests that MU69 is either nearly spherical (a:b axis ratio of 1:1.15), or its pole vector is pointed near the line of sight to Earth; this interpretation does not preclude a near-contact binary or bi-lobed object. However, image stacks do conclude that MU69 does not have a binary companion ≥2000 km with a sensitivity to 29th magnitude (an object a few km in size for an albedo of 0.04–0.15). Our data are not of sufficient signal to noise to uniquely determine the period or amplitude, however, they did provide the necessary information for spacecraft planning. We report with confidence that MU69 is not both rapidly rotating *and* highly elongated (which we define as a lightcurve amplitude ≥ 0.5 magnitude). Since this paper is being published post fly-by, we note that our results are consistent with the fly-by imagery and orientation of MU69 (Stern et al., 2019). The combined dataset also suggests that within the KBO lightcurve literature there are likely other objects which share a geometric configuration like MU69 resulting in an underestimate of the contact binary fraction for the Cold Classical Kuiper Belt.

1. Introduction

(486958) 2014 MU_{69} "Ultima Thule" (hereafter MU69) is one of ~3000 objects that have thus far been identified and cataloged since discovery of the first Kuiper Belt object in 1992 (Jewitt and Luu, 1993). MU69 resides in the Cold Classical region of the Kuiper Belt with a semi-major axis of a = 44.08 AU, a nearly circular orbit with e = 0.035, and low inclination of i = 2.4°. MU69 was one of 5 objects discovered through a deep, directed search for a post-Pluto fly-by target for the *New Horizons* spacecraft (Stern et al., 2018) using the *Hubble Space Telescope* (HST) in the summer of 2014 [GO-13663; PI J. Spencer; see also Buie et al. (2018a, 2018b)]. Follow-up astrometric measurements (GO-14485, GO-14629, and GO-15158; PI M. Buie) confirmed its suitability for flyby accessibility, and refined its orbit for spacecraft targeting (Porter et al., 2018). Along with positional information we also acquired photometry, although at differing signal-to-noise ratios (S/N) depending on the observational geometry dictated by the need for orbit refinement. All of the data were collected using the Wide Field Camera 3 (WFC3) in the F350LP filter in order to collect as many photons as possible on the object. Exposures for the astrometric images were 368 s in duration.

While the *New Horizons* flyby provided a close, detailed understanding of MU69, precise encounter planning and navigation depended on the ability to characterize its physical properties from the confines of the Earth and Earth's orbit. HST has ideal capabilities to

* Corresponding author.
E-mail address: susank@psi.edu (S.D. Benecchi).

https://doi.org/10.1016/j.icarus.2019.01.023
Received 8 December 2018; Received in revised form 22 January 2019; Accepted 28 January 2019
Available online 31 January 2019
0019-1035/ © 2019 The Authors. Published by Elsevier Inc. This is an open access article under the CC BY-NC-ND license (http://creativecommons.org/licenses/by-nc-nd/4.0/).

Table 1
Photometry from HST astrometry campaigns.

Rootname	JD (midtime)	Light-time corrected JD (midtime)	ST_mag	Vega_mag	Magerr	R (au)	Δ (au)	α(°)	1-wayLT	H_{ST_mag}
icii11r7q_1	2456834.86924	2456834.62440	27.17	26.85	0.14	43.41	42.40	0.148	352.570	10.43
icii11raq_1	2456834.88153	2456834.63669	27.43	27.11	0.17	43.41	42.40	0.148	352.570	10.69
icii11rcq_1	2456834.88768	2456834.64284	27.33	27.01	0.15	43.41	42.40	0.148	352.570	10.59
icii11req_1	2456834.89382	2456834.64898	27.41	27.09	0.15	43.41	42.40	0.148	352.570	10.66
icii12rqq_1	2456835.00812	2456834.76328	27.13	26.81	0.13	43.41	42.40	0.145	352.570	10.39
icii12rsq_1	2456835.01426	2456834.76942	27.46	27.14	0.17	43.41	42.40	0.145	352.570	10.72
icii12ruq_1	2456835.02041	2456834.77557	27.38	27.06	0.16	43.41	42.40	0.145	352.570	10.64
iciig7cwq_2	2456872.04538	2456871.79980	27.54	27.22	0.18	43.41	42.53	0.676	353.627	10.69
iciig7cyq_2	2456872.05152	2456871.80595	27.41	27.09	0.17	43.41	42.53	0.676	353.627	10.57
iciig7d0q_2	2456872.05767	2456871.81209	27.16	26.84	0.13	43.41	42.53	0.676	353.627	10.32
iciig7d2q_2	2456872.06381	2456871.81824	27.43	27.11	0.17	43.41	42.53	0.676	353.627	10.58
iciig8kaq_2	2456873.23983	2456872.99420	27.03	26.71	0.12	43.41	42.54	0.699	353.710	10.18
iciig8kcq_2	2456873.24598	2456873.00035	27.41	27.09	0.16	43.41	42.54	0.699	353.710	10.56
iciig8keq_2	2456873.25212	2456873.00649	27.81	27.49	0.22	43.41	42.54	0.699	353.710	10.96
iciig9ryq_2	2456890.83129	2456890.58456	27.86	27.54	0.24	43.41	42.73	1.002	355.298	10.95
iciig9s0q_2	2456890.83744	2456890.59070	27.50	27.18	0.18	43.41	42.73	1.002	355.298	10.59
iciig9s2q_2	2456890.84358	2456890.59685	27.43	27.11	0.16	43.41	42.73	1.002	355.298	10.52
iciih0s4q_2	2456890.88535	2456890.63861	27.65	27.33	0.21	43.41	42.73	1.002	355.306	10.74
iciih0s5q_2	2456890.89150	2456890.64476	27.64	27.32	0.20	43.41	42.73	1.003	355.306	10.73
iciih0s7q_2	2456890.89764	2456890.65090	27.53	27.21	0.18	43.41	42.73	1.003	355.306	10.61
iciih0s9q_2	2456890.90379	2456890.65705	27.45	27.13	0.16	43.41	42.73	1.003	355.306	10.54
iciih0sbq_2	2456890.90994	2456890.66320	27.23	26.91	0.15	43.41	42.73	1.003	355.306	10.32
iciih3byq_2	2456892.67695	2456892.43008	27.47	27.15	0.19	43.41	42.75	1.029	355.498	10.56
iciih3bzq_2	2456892.68310	2456892.43622	27.38	27.06	0.18	43.41	42.75	1.029	355.498	10.46
iciih3c1q_2	2456892.68924	2456892.44237	27.55	27.23	0.19	43.41	42.75	1.029	355.498	10.63
iciih3c3q_2	2456892.69539	2456892.44851	27.83	27.51	0.25	43.41	42.75	1.029	355.498	10.91
iciih3c5q_2	2456892.70153	2456892.45466	27.46	27.14	0.18	43.41	42.75	1.029	355.498	10.55
iciih4c7q_2	2456892.74332	2456892.49644	27.27	26.95	0.16	43.41	42.75	1.030	355.506	10.35
iciih4c8q_2	2456892.74946	2456892.50258	27.28	26.96	0.15	43.41	42.75	1.030	355.506	10.37
iciih4caq_2	2456892.75561	2456892.50873	27.29	26.97	0.15	43.41	42.75	1.030	355.506	10.38
iciih4ccq_2	2456892.76175	2456892.51487	27.81	27.49	0.23	43.41	42.75	1.030	355.506	10.89
iciij5yfq_2	2456945.57313	2456945.32139	27.87	27.55	0.28	43.40	43.59	1.291	362.516	10.86
iciij5yjq_2	2456945.58542	2456945.33368	27.36	27.04	0.18	43.40	43.59	1.291	362.516	10.35
iciij6yyq_2	2456945.64563	2456945.39388	27.65	27.33	0.23	43.40	43.60	1.291	362.524	10.64
iciij6z2q_2	2456945.65792	2456945.40617	27.33	27.01	0.18	43.40	43.60	1.291	362.533	10.32
iciij7etq_2	2456946.69482	2456946.44297	27.60	27.28	0.24	43.40	43.61	1.285	362.674	10.59
iciij7eyq_2	2456946.71326	2456946.46140	27.53	27.21	0.21	43.40	43.61	1.285	362.674	10.53
iciij9c7q_2	2456952.87053	2456952.61809	27.49	27.17	0.22	43.40	43.71	1.245	363.514	10.48
iciij9c9q_2	2456952.87667	2456952.62423	27.58	27.26	0.21	43.40	43.71	1.245	363.514	10.57
ict101egq_2	2457147.19178	2457146.94431	27.51	27.19	0.18	43.38	42.85	1.137	356.362	10.57
ict101eiq_2	2457147.19791	2457146.95043	27.65	27.33	0.19	43.38	42.85	1.137	356.362	10.71
ict103vwq_2	2457208.11057	2457207.86594	27.30	26.98	0.17	43.38	42.36	0.052	352.271	10.58
ict103vyq_2	2457208.11670	2457207.87207	27.47	27.15	0.18	43.38	42.36	0.052	352.271	10.75
ict103w0q_2	2457208.12284	2457207.87821	27.30	26.98	0.14	43.38	42.36	0.052	352.271	10.57
ict103w2q_2	2457208.12897	2457207.88434	27.35	27.03	0.15	43.38	42.36	0.052	352.271	10.63
id3m01hhq_2	2457462.50829	2457462.25608	27.62	27.30	0.24	43.36	43.67	1.236	363.181	10.62
id3m01hiq_2	2457462.51440	2457462.26219	28.01	27.69	0.32	43.36	43.67	1.236	363.181	11.01
id3m01hsq_2	2457462.53273	2457462.28052	27.63	27.31	0.27	43.36	43.67	1.236	363.181	10.63
id3m02snq_2	2457523.59107	2457523.34455	27.28	26.96	0.14	43.35	42.69	1.009	354.982	10.37
id3m02soq_2	2457523.59718	2457523.35066	27.86	27.54	0.22	43.35	42.69	1.009	354.982	10.95
id3m02sqq_2	2457523.60329	2457523.35678	27.63	27.31	0.19	43.35	42.69	1.009	354.982	10.72
id3m02suq_2	2457523.61551	2457523.36900	26.76	26.44	0.11	43.35	42.69	1.008	354.982	9.85
id5901erq_2	2457595.20717	2457594.96235	27.35	27.03	0.16	43.35	42.39	0.475	352.537	10.56
id5901etq_2	2457595.21328	2457594.96846	27.31	26.99	0.15	43.35	42.39	0.475	352.537	10.51
id5901evq_2	2457595.21939	2457594.97458	27.17	26.85	0.14	43.35	42.39	0.475	352.537	10.38
id5901exq_2	2457595.22550	2457594.98069	27.86	27.54	0.24	43.35	42.39	0.475	352.537	11.06
id5902a9q_2	2457682.71348	2457682.46169	27.42	27.10	0.20	43.34	43.60	1.271	362.583	10.42
id5902adq_2	2457682.72570	2457682.47390	27.56	27.24	0.23	43.34	43.60	1.271	362.591	10.55
id5902afq_2	2457682.73181	2457682.48001	27.78	27.46	0.26	43.34	43.60	1.271	362.591	10.78
id5953gxq_2	2457875.37689	2457875.12932	27.21	26.89	0.14	43.32	42.87	1.191	356.504	10.26
id5953gyq_2	2457875.38300	2457875.13543	27.29	26.97	0.13	43.32	42.87	1.191	356.504	10.34
id5953h0q_2	2457875.38911	2457875.14154	27.20	26.88	0.14	43.32	42.87	1.191	356.504	10.25
id5953h2q_2	2457875.39523	2457875.14765	27.30	26.98	0.14	43.32	42.87	1.190	356.504	10.35
id5953h4q_2	2457875.40134	2457875.15376	27.60	27.28	0.19	43.32	42.87	1.190	356.504	10.65
id5904wiq_2	2457899.22773	2457898.98201	27.48	27.16	0.15	43.32	42.55	0.866	353.826	10.60
id5904wkq_2	2457899.23384	2457898.98812	27.32	27.00	0.14	43.32	42.55	0.866	353.826	10.44
id5904wmq_2	2457899.23995	2457898.99424	27.41	27.09	0.15	43.32	42.55	0.866	353.826	10.54
id5906kaq_2	2457985.11989	2457984.87404	27.54	27.22	0.17	43.31	42.57	0.920	354.026	10.65
id5906kbq_2	2457985.12600	2457984.88015	27.42	27.10	0.16	43.31	42.57	0.920	354.026	10.54
id5906kdq_2	2457985.13211	2457984.88626	27.58	27.26	0.18	43.31	42.57	0.920	354.026	10.69
id5906khq_2	2457985.14434	2457984.89849	27.53	27.21	0.17	43.31	42.57	0.920	354.026	10.64
idoy07yuq_2	2458054.06655	2458053.81447	27.19	26.87	0.16	43.31	43.65	1.235	362.998	10.20
idoy07ywq_2	2458054.07266	2458053.82058	27.70	27.38	0.25	43.31	43.65	1.235	362.998	10.71

(*continued on next page*)

Table 1 (*continued*)

Rootname	JD (midtime)	Light-time corrected JD (midtime)	ST_mag	Vega_mag	Magerr	R (au)	Δ (au)	α(°)	1-wayLT	H_{ST_mag}
idoy07yyq_2	2458054.07877	2458053.82669	27.03	26.71	0.15	43.31	43.65	1.235	362.998	10.04
idoy07z0q_2	2458054.08488	2458053.83280	27.67	27.35	0.25	43.31	43.65	1.235	362.998	10.67
idoy08idq_2	2458193.59001	2458193.33794	27.91	27.59	0.28	43.30	43.65	1.223	362.982	10.92
idoy09jdq_2	2458259.27628	2458259.03028	27.42	27.10	0.15	43.29	42.60	0.975	354.242	10.52
idoy09jfq_2	2458259.28239	2458259.03639	27.39	27.07	0.15	43.29	42.60	0.975	354.242	10.49
idoy10ktq_2	2458321.12211	2458320.87783	27.40	27.08	0.16	43.29	42.30	0.315	351.772	10.64
idoy10kvq_2	2458321.12822	2458320.88394	26.99	26.67	0.11	43.29	42.30	0.315	351.772	10.23
idoy10kxq_2	2458321.13433	2458320.89005	27.61	27.29	0.19	43.29	42.30	0.315	351.772	10.85
idoy10kzq_2	2458321.14045	2458320.89616	27.05	26.73	0.12	43.29	42.30	0.315	351.772	10.29
idoy11f5q_2	2458356.89321	2458356.64716	27.60	27.28	0.17	43.28	42.61	0.999	354.317	10.71
idoy11f7q_2	2458356.89932	2458356.65327	27.82	27.50	0.20	43.28	42.61	1.000	354.317	10.92
idw612qsq_2	2458430.30320	2458430.05042	26.61	26.29	0.13	43.28	43.77	1.136	364.005	9.63
idw612qvq_2	2458430.31543	2458430.06265	27.35	27.03	0.21	43.28	43.77	1.136	364.005	10.36

accomplish these flyby precursor support tasks. One of the key physical characteristics to investigate was MU69's shape and/or binary nature. If MU69 were significantly elongated, then the *New Horizons* team would want to time the close encounter to take place when the largest cross-section faces the spacecraft. Likewise, if the object were found to be rotating rapidly, then that rotation period could have influenced the instrument sequencing and integration times.

2. Photometry from astrometric dataset

Our search for rotational variation began by using photometry extracted from the HST astrometric dataset (Table 1, see Section 4 for details of photometry extraction). Since the data were collected near both points of quadrature as well as at opposition, the data span a wide range of S/N. We geometrically correct the photometry to an H-magnitude, H_{F350LP}, following the relations of Bowell et al. (1989) modified for a linear phase function:

$$H_{F350LP} = m_{F350LP}(1, 1, \alpha = 0^{\circ}) = mF_{350LP} - 5\log(r\Delta) - \alpha\beta. \quad (1)$$

In Eq. (1), r and Δ (in AU) are the heliocentric and geocentric, distances, respectively, α is the solar phase angle β is the solar phase coefficient. We consider the linear phase function appropriate because of the low the S/N of the data. Our data cover a phase range from 0.05° to 1.29° and we find a phase coefficient of $\beta = 0.18 \pm 0.01$ mag/° (Fig. 1) determined by a linear fit to the non-phased, but geometrically corrected, data combining all of the measurements available. The resulting, corrected, photometry for MU69 is plotted in Fig. 2.

We used this astrometric dataset to place constraints on the amplitude of possible lightcurves because the wide spacing of the astrometric dataset is not suited for rotation-period determination. The uncertainties in this dataset are sizable, with a mean of 0.18 magnitudes, but sometimes as large as 0.32 magnitudes. Magnitude variations within individual HST orbits average around 0.15 magnitudes, but are as large as 0.4 magnitudes and not always systematic. Given the large range of S/N in this dataset we reasoned that variations of ≥0.3 magnitudes provided an approximate lower limit for the lightcurve amplitude of MU69 to be expected in a more densely sampled survey. This is a lower limit because assuming the rotation period is longer than 3.2 h (2 consecutive HST orbits), a reasonable assumption for KBOs (Romanishin and Tegler, 1999), then at best we are only observing part of the rise or fall in the lightcurve amplitude during the astrometric observations.

To place our assumptions in context, we note that the average rotation period for KBOs, with some degeneracy with respect to single vs. double peaked lightcurve interpretations, ranges from 7 to 9 h (Duffard et al., 2009; Benecchi and Sheppard, 2013; Thirouin et al., 2016). However, periods as short as 3.9 h (Haumea; Rabinowitz et al., 2006) and as long as 154 h (Pluto-Charon; Walker and Hardie, 1955) have been measured, so the 99 sparsely-measured points spaced over 4 years do not provide sufficiently dense sampling. We used the range of observed periods as a guide when designing our survey.

3. New observations

Armed only with the knowledge that the total flux from MU69 varies, we set out to design an HST program to attempt to extract its rotation period and amplitude. Without prior information about how short or long the rotation period might be, we designed a program (GO-14627; PI S. Benecchi) to sample periods ranging from a few to multiple tens of hours. We assumed that the object is more likely elongated rather than spherical given our knowledge of small KBO lightcurves thus far (Trilling and Bernstein, 2006). If we measure large amplitude (> 0.4 magnitudes) variation then we will be able to more reliably estimate MU69's true rotation. If, however, the lightcurve amplitude is small, then there is likely to be some ambiguity in the true period determination (Harris et al., 2014). In either case, our experiment was designed to provide useful constraints for spacecraft planning.

Our measurement sequence utilized 4 visits of 6 HST orbits for a total of 24 orbits within the timespan of 224.66 h (based on exposure mid-times; 9.36 days), near opposition, between June 25 and July 4, when MU69 should be brightest. Visit 1 spanned 10.12 h and was

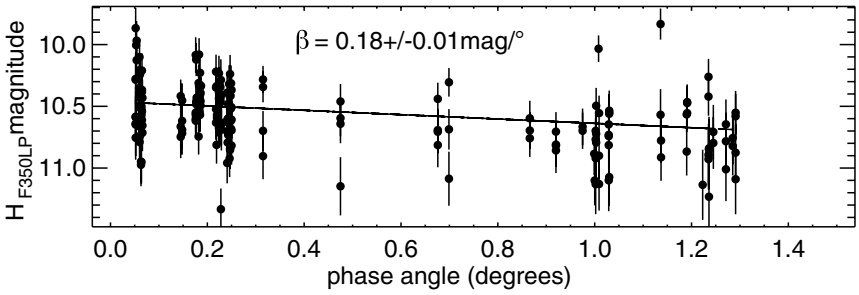

Fig. 1. Linear fit to the non-phase, but geometrically corrected, data (1-sigma error bars are plotted) combining all of the measurements acquired over 4 years. The resulting phase coefficient is $\beta = 0.18 \pm 0.01$ mag/deg.

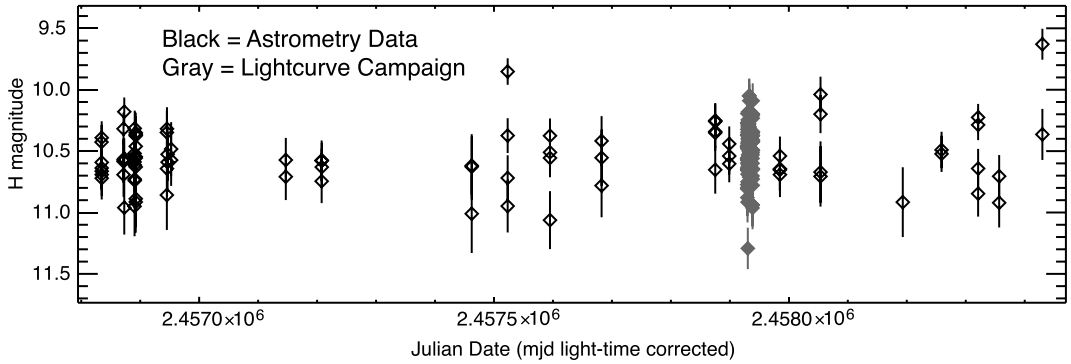

Fig. 2. Geometrically corrected photometry from astrometric (black open points) and lightcurve (gray filled points) measurements 2014–2018 (1-sigma error bars plotted). The combined dataset covers 4 years while the lightcurve data are concentrated over 9.36 days. Although there is quite a bit of scatter in the data and we cannot determine the period, it would be possible to hide a lightcurve amplitude of up to 0.6 magnitudes within this dataset.

separated from Visit 2 by 13.7 h (0.57 days). Visit 2 spanned 11.65 h, and was separated from visit 3 by 34.3 h (1.4 days). Visit 3 spanned 11.71 h and was separated from visit 4 by 131.3 h (5.47 days). Visit 4 spanned 11.7 h. The orbits within a visit were as consecutive as possible, in order to minimize aliasing interpretations of the period; however, HST gyroscope limitations require the telescope to move off the MU69 field after 3–4 consecutive orbits. Therefore, all of the visit orbit sequences have a one or two orbit gap someplace within them. Using synthetic lightcurve datasets we concluded prior to scheduling that these gaps would not significantly impact the ability to interpret our results. The HST fields were examined in advance for background sources to make sure that we optimized the photometric return and minimized contaminated observations. Data were collected in the F350LP filter to obtain the highest S/N possible (as good as S/N~7 in the actual dataset) with integrations of 367 s in duration, allowing for 5 exposures in each HST orbit.

4. Photometry from lightcurve dataset

Photometry was carried out with an IDL PSF-Tiny Tim (Krist and Hook, 2004) matching routine which uses an amoeba (Press et al., 1992) downhill simplex method minimization to match the model to the data by iteratively adjusting the values of the fitted parameters until the χ^2 converged (Benecchi et al., 2009). Due to the low S/N of the data ~10 iterations, which we checked as the conversion happened to make sure that the model was not stuck on any background variations, were typically required to reach a final PSF model.

Initially each image was modelled with both a single and double PSF (fitting for x1,y1, flux1 in one case and x1,y1,flux1,x2,y2,flux2 in the second case) in addition to fitting for the sky background. Likewise, we also fit single and double PSFs to the orbit, visit, and campaign stacked images to look for a binary companion.

Next we ran a photometric analysis where instead of deriving the (x,y) position from the images themselves, we forced the (x,y) position on each image to be that projected by the best orbit solution for MU69 (Porter et al., 2018). In this case we fit for only the object flux and sky background. This seemed the best way to consistently extract the fluxes for all of the HST data available for MU69 independent of the original purpose for the observations, especially since some of the measurements in the astrometric campaign were barely detectable.

The calibrated fluxes (Table 2), expressed in the ST-magnitude (STMAG) and Vega-magnitude (VEGAMAG) systems, were derived from the observed counts matched to the actual MU69 images for an infinite aperture on the Tiny Tim models using the inverse sensitivity and photometric zero point keyword values (PHOTFLAM and PHOTZPT) from the HST image headers (Rajan et al., 2011). Photometry is extracted from the model data to remove noise from background sources that increase the background signal and respective uncertainty in the raw images. To estimate uncertainty on the flux itself we re-run the data/model comparison with steps in flux to determine the value at which the χ^2 residual of the image changes by 1-sigma. Fig. 3 shows the results in F350LP ST-magnitudes for each of the individual lightcurve campaign visits. For reference this Vega-magnitude system (the reference system for most ground-based measurements) is 0.321 magnitudes brighter than the ST-magnitude system (http://www.stsci.edu/hst/wfc3/analysis/uvis_zpts/uvis1_infinite).

5. Data analysis

5.1. Binary evaluation

MU69 was easily identified in individual exposures; in most cases there were no obvious background sources or nearby bright stars. From the results of the binary vs. single image PSF fits, we conclude that MU69 is not a resolved binary in the individual HST images.

Additionally we stacked the images within each orbit to search for fainter companions that might have been missed in the individual image analysis. Images from each HST orbit (5 images per orbit, with orbit 12 having only 4 images due to an HST timing constraint), each visit (30 images over 6 orbits), and from the entire lightcurve campaign (119 images) were stacked to search for faint companions (Fig. 4). We then re-ran our PSF fitting code as described in section 4 on each of the stacks. No faint companions were identified. Therefore, we can say with confidence that MU69 does not have a binary companion separated by $\geq$2000 km, with a sensitivity to 29th magnitude. This limit corresponds to an object a few km in size for an assumed albedo of 0.15–0.04.

5.2. Lightcurve extraction

We ran two sets of analyses on the extracted magnitudes from our survey data: one considered data from only the new lightcurve campaign [119 images in total spanning 224.66 h (9.36 days)] and a second considered all of the photometry available for MU69 (an additional 99 images made since 2014), yielding a 4-year baseline (Fig. 1, bottom). To put all these data on the same baseline, we geometrically corrected all of the data (Table 2) following the same process as that described in Section 2. The caveat for this second analysis is that the uncertainties at some epochs are large, so when we fit a period to the data we weight the points by their uncertainties and when we evaluate the amplitude of a potential lightcurve we only consider the lightcurve campaign data since they have both high S/N as well as the appropriate time sampling for lightcurve work. All of our analysis is done using light-time corrected times-stamps derived from the observation Julian date mid-times from the images corrected for the observing geometry as provided in Tables 1 & 2.

We analyze the data using a modified Phase Dispersion Minimization (PDM; Stellingwerf, 1978) fitting technique that goes

Table 2
Photometry from HST lightcurve campaign.

Image rootname	JD (midtime)	Light-time corrected JD (midtime)	ST_mag	Vega_mag	Magerr	R (au)	Δ (au)	α(°)	1-wayLT	H_{ST_mag}
id8i01skq	2457929.81763	2457929.57322	27.01	26.69	0.15	43.32	42.32	0.250	351.947	10.65
id8i01slq	2457929.82375	2457929.57934	26.82	26.50	0.15	43.32	42.32	0.250	351.947	10.46
id8i01snq	2457929.82986	2457929.58545	27.13	26.81	0.15	43.32	42.32	0.250	351.947	10.77
id8i01spq	2457929.83597	2457929.59156	26.92	26.60	0.15	43.32	42.32	0.250	351.947	10.56
id8i01srq	2457929.84208	2457929.59767	26.68	26.36	0.15	43.32	42.32	0.250	351.947	10.32
id8i02stq	2457929.88385	2457929.63944	26.93	26.61	0.15	43.32	42.32	0.249	351.947	10.57
id8i02suq	2457929.88996	2457929.64555	27.00	26.68	0.15	43.32	42.32	0.249	351.947	10.64
id8i02swq	2457929.89607	2457929.65166	26.63	26.31	0.15	43.32	42.32	0.249	351.947	10.27
id8i02syq	2457929.90218	2457929.65777	26.83	26.51	0.15	43.32	42.32	0.249	351.947	10.47
id8i02t0q	2457929.90829	2457929.66388	26.73	26.41	0.15	43.32	42.32	0.248	351.947	10.37
id8i03t4q	2457929.95006	2457929.70566	27.17	26.85	0.16	43.32	42.32	0.247	351.938	10.81
id8i03t7q	2457929.95618	2457929.71178	26.84	26.52	0.16	43.32	42.32	0.247	351.938	10.48
id8i03t9q	2457929.96229	2457929.71789	26.82	26.50	0.16	43.32	42.32	0.247	351.938	10.46
id8i03tbq	2457929.96840	2457929.72400	26.55	26.23	0.16	43.32	42.32	0.247	351.938	10.19
id8i03tdq	2457929.97451	2457929.73011	27.16	26.84	0.16	43.32	42.32	0.247	351.938	10.80
id8i04tfq	2457930.01629	2457929.77189	26.81	26.49	0.15	43.32	42.32	0.246	351.938	10.45
id8i04tgq	2457930.02240	2457929.77800	27.24	26.92	0.15	43.32	42.32	0.246	351.938	10.88
id8i04tiq	2457930.02851	2457929.78411	26.73	26.41	0.15	43.32	42.32	0.246	351.938	10.37
id8i04tkq	2457930.03463	2457929.79023	26.96	26.64	0.15	43.32	42.32	0.245	351.938	10.60
id8i04tmq	2457930.04074	2457929.79634	26.64	26.32	0.15	43.32	42.32	0.245	351.938	10.27
id8i05txq	2457930.14873	2457929.90433	26.93	26.61	0.09	43.32	42.32	0.243	351.938	10.57
id8i05tyq	2457930.15484	2457929.91044	26.92	26.60	0.09	43.32	42.32	0.243	351.938	10.56
id8i05u0q	2457930.16096	2457929.91656	26.80	26.48	0.09	43.32	42.32	0.243	351.938	10.44
id8i05u2q	2457930.16707	2457929.92267	26.91	26.59	0.09	43.32	42.32	0.243	351.938	10.55
id8i05u4q	2457930.17318	2457929.92878	27.05	26.73	0.09	43.32	42.32	0.243	351.938	10.69
id8i06u6q	2457930.21494	2457929.97054	27.11	26.79	0.17	43.32	42.32	0.242	351.938	10.75
id8i06u7q	2457930.22105	2457929.97665	26.93	26.61	0.17	43.32	42.32	0.241	351.938	10.57
id8i06u9q	2457930.22716	2457929.98276	26.71	26.39	0.17	43.32	42.32	0.241	351.938	10.35
id8i06ubq	2457930.23327	2457929.98887	27.28	26.96	0.17	43.32	42.32	0.241	351.938	10.92
id8i06udq	2457930.23938	2457929.99498	27.02	26.70	0.17	43.32	42.32	0.241	351.938	10.66
id8i07crq	2457930.81090	2457930.56651	27.01	26.69	0.17	43.32	42.32	0.229	351.922	10.65
id8i07ctq	2457930.81701	2457930.57262	26.96	26.64	0.17	43.32	42.32	0.229	351.922	10.60
id8i07cwq	2457930.82312	2457930.57873	26.60	26.28	0.17	43.32	42.32	0.228	351.922	10.25
id8i07cyq	2457930.82923	2457930.58484	27.65	27.33	0.17	43.32	42.32	0.228	351.922	11.29
id8i07d1q	2457930.83534	2457930.59095	26.73	26.41	0.17	43.32	42.32	0.228	351.922	10.38
id8i08daq	2457930.87713	2457930.63274	27.00	26.68	0.13	43.32	42.32	0.227	351.922	10.64
id8i08dbq	2457930.88324	2457930.63885	26.76	26.44	0.13	43.32	42.32	0.227	351.922	10.40
id8i08ddq	2457930.88935	2457930.64496	26.78	26.46	0.13	43.32	42.32	0.227	351.922	10.43
id8i08dfq	2457930.89546	2457930.65107	26.78	26.46	0.13	43.32	42.32	0.227	351.922	10.42
id8i08diq	2457930.90157	2457930.65718	26.66	26.34	0.13	43.32	42.32	0.227	351.922	10.30
id8i09dkq	2457930.94335	2457930.69897	26.71	26.39	0.14	43.32	42.32	0.226	351.913	10.36
id8i09dlq	2457930.94946	2457930.70508	27.00	26.68	0.14	43.32	42.32	0.225	351.913	10.65
id8i09dnq	2457930.95557	2457930.71119	26.64	26.32	0.14	43.32	42.32	0.225	351.913	10.29
id8i09dpq	2457930.96169	2457930.71731	26.98	26.66	0.14	43.32	42.32	0.225	351.913	10.63
id8i09drq	2457930.96780	2457930.72342	26.64	26.32	0.14	43.32	42.32	0.225	351.913	10.29
id8i10dtq	2457931.00957	2457930.76519	26.99	26.67	0.14	43.32	42.32	0.224	351.913	10.64
id8i10duq	2457931.01568	2457930.77130	26.70	26.38	0.14	43.32	42.32	0.224	351.913	10.35
id8i10dwq	2457931.02179	2457930.77741	26.55	26.23	0.14	43.32	42.32	0.224	351.913	10.19
id8i10dyq	2457931.02790	2457930.78352	26.75	26.43	0.14	43.32	42.32	0.224	351.913	10.40
id8i10e0q	2457931.03401	2457930.78963	26.94	26.62	0.14	43.32	42.32	0.224	351.913	10.58
id8i11ejq	2457931.21489	2457930.97051	26.89	26.57	0.15	43.32	42.32	0.220	351.913	10.53
id8i11elq	2457931.22100	2457930.97662	26.91	26.59	0.15	43.32	42.32	0.220	351.913	10.55
id8i11eoq	2457931.22711	2457930.98273	27.13	26.81	0.15	43.32	42.32	0.219	351.913	10.77
id8i11eqq	2457931.23322	2457930.98884	26.65	26.33	0.15	43.32	42.32	0.219	351.913	10.30
id8i12esq	2457931.27804	2457931.03366	26.95	26.63	0.14	43.32	42.32	0.218	351.905	10.59
id8i12etq	2457931.28415	2457931.03977	26.54	26.22	0.14	43.32	42.32	0.218	351.905	10.18
id8i12evq	2457931.29026	2457931.04588	26.66	26.34	0.14	43.32	42.32	0.218	351.905	10.31
id8i12exq	2457931.29637	2457931.05199	26.84	26.52	0.14	43.32	42.32	0.218	351.905	10.48
id8i13lvq	2457932.73121	2457932.48685	26.65	26.33	0.07	43.32	42.32	0.187	351.880	10.30
id8i13lwq	2457932.73732	2457932.49296	26.66	26.34	0.07	43.32	42.32	0.186	351.880	10.31
id8i13lyq	2457932.74343	2457932.49907	26.77	26.45	0.07	43.32	42.32	0.186	351.880	10.42
id8i13m0q	2457932.74954	2457932.50518	26.81	26.49	0.07	43.32	42.32	0.186	351.880	10.46
id8i13m3q	2457932.75566	2457932.51130	26.71	26.39	0.07	43.32	42.32	0.186	351.880	10.36
id8i14m5q	2457932.79743	2457932.55307	26.54	26.22	0.14	43.32	42.31	0.185	351.872	10.20
id8i14m6q	2457932.80354	2457932.55918	26.72	26.40	0.14	43.32	42.31	0.185	351.872	10.37
id8i14m8q	2457932.80965	2457932.56529	26.88	26.56	0.14	43.32	42.31	0.185	351.872	10.54
id8i14maq	2457932.81576	2457932.57140	26.88	26.56	0.14	43.32	42.31	0.184	351.872	10.53
id8i14mcq	2457932.82187	2457932.57751	26.75	26.43	0.14	43.32	42.31	0.184	351.872	10.40
id8i15meq	2457932.86363	2457932.61927	26.85	26.53	0.13	43.32	42.31	0.184	351.872	10.50
id8i15mfq	2457932.86974	2457932.62538	26.75	26.43	0.13	43.32	42.31	0.184	351.872	10.40
id8i15mhq	2457932.87585	2457932.63149	26.40	26.08	0.13	43.32	42.31	0.183	351.872	10.05
id8i15mjq	2457932.88196	2457932.63760	26.77	26.45	0.13	43.32	42.31	0.183	351.872	10.42
id8i15mlq	2457932.88807	2457932.64371	26.65	26.33	0.13	43.32	42.31	0.183	351.872	10.30

(*continued on next page*)

Table 2 (*continued*)

Image rootname	JD (midtime)	Light-time corrected JD (midtime)	ST_mag	Vega_mag	Magerr	R (au)	Δ (au)	α(°)	1-wayLT	H_{ST_mag}
id8i16mnq	2457932.92986	2457932.68550	27.06	26.74	0.15	43.32	42.31	0.182	351.872	10.71
id8i16moq	2457932.93597	2457932.69161	26.63	26.31	0.15	43.32	42.31	0.182	351.872	10.28
id8i16mqq	2457932.94208	2457932.69772	26.80	26.48	0.15	43.32	42.31	0.182	351.872	10.45
id8i16msq	2457932.94819	2457932.70383	26.81	26.49	0.15	43.32	42.31	0.182	351.872	10.46
id8i16muq	2457932.95430	2457932.70994	26.85	26.53	0.15	43.32	42.31	0.182	351.872	10.50
id8i17obq	2457933.12850	2457932.88414	26.77	26.45	0.13	43.32	42.31	0.178	351.872	10.42
id8i17ocq	2457933.13461	2457932.89025	26.80	26.48	0.13	43.32	42.31	0.178	351.872	10.45
id8i17oeq	2457933.14072	2457932.89636	26.75	26.43	0.13	43.32	42.31	0.178	351.872	10.40
id8i17ogq	2457933.14684	2457932.90248	26.78	26.46	0.13	43.32	42.31	0.177	351.872	10.44
id8i17oiq	2457933.15295	2457932.90859	26.44	26.12	0.13	43.32	42.31	0.177	351.872	10.09
id8i18okq	2457933.19472	2457932.95036	26.88	26.56	0.14	43.32	42.31	0.176	351.872	10.54
id8i18olq	2457933.20083	2457932.95648	26.87	26.55	0.14	43.32	42.31	0.176	351.864	10.52
id8i18onq	2457933.20694	2457932.96259	26.92	26.60	0.14	43.32	42.31	0.176	351.864	10.57
id8i18opq	2457933.21305	2457932.96870	26.40	26.08	0.14	43.32	42.31	0.176	351.864	10.05
id8i18orq	2457933.21916	2457932.97481	26.93	26.61	0.14	43.32	42.31	0.176	351.864	10.59
id8i19geq	2457938.69074	2457938.44644	26.97	26.65	0.15	43.32	42.31	0.066	351.797	10.64
id8i19gfq	2457938.69685	2457938.45255	27.03	26.71	0.15	43.32	42.31	0.066	351.797	10.70
id8i19gpq	2457938.70296	2457938.45866	26.75	26.43	0.15	43.32	42.31	0.066	351.797	10.42
id8i19grq	2457938.70907	2457938.46477	26.68	26.36	0.15	43.32	42.31	0.065	351.797	10.36
id8i19gtq	2457938.71518	2457938.47088	26.93	26.61	0.15	43.32	42.31	0.065	351.797	10.60
id8i20h2q	2457938.75695	2457938.51265	26.86	26.54	0.14	43.32	42.31	0.065	351.797	10.53
id8i20h3q	2457938.76306	2457938.51876	26.70	26.38	0.14	43.32	42.31	0.065	351.797	10.37
id8i20h5q	2457938.76917	2457938.52487	26.53	26.21	0.14	43.32	42.31	0.065	351.797	10.20
id8i20h7q	2457938.77528	2457938.53098	26.84	26.52	0.14	43.32	42.31	0.064	351.797	10.51
id8i20h9q	2457938.78140	2457938.53710	26.89	26.57	0.14	43.32	42.31	0.064	351.797	10.56
id8i21hbq	2457938.82319	2457938.57889	27.27	26.95	0.17	43.32	42.31	0.064	351.797	10.94
id8i21hcq	2457938.82930	2457938.58500	26.81	26.49	0.17	43.32	42.31	0.064	351.797	10.49
id8i21heq	2457938.83541	2457938.59111	27.29	26.97	0.17	43.32	42.31	0.063	351.797	10.96
id8i21hgq	2457938.84152	2457938.59722	27.26	26.94	0.17	43.32	42.31	0.063	351.797	10.94
id8i21hiq	2457938.84763	2457938.60333	26.75	26.43	0.17	43.32	42.31	0.063	351.797	10.43
id8i22hyq	2457939.02184	2457938.77754	26.56	26.24	0.13	43.32	42.31	0.061	351.797	10.23
id8i22hzq	2457939.02795	2457938.78365	26.73	26.41	0.13	43.32	42.31	0.061	351.797	10.41
id8i22i1q	2457939.03406	2457938.78976	26.54	26.22	0.13	43.32	42.31	0.061	351.797	10.21
id8i22i3q	2457939.04017	2457938.79587	27.05	26.73	0.13	43.32	42.31	0.061	351.797	10.73
id8i22i5q	2457939.04628	2457938.80198	26.52	26.20	0.13	43.32	42.31	0.060	351.797	10.20
id8i23i7q	2457939.08806	2457938.84376	26.67	26.35	0.14	43.32	42.31	0.060	351.797	10.34
id8i23i8q	2457939.09417	2457938.84987	26.42	26.10	0.14	43.32	42.31	0.060	351.797	10.09
id8i23iaq	2457939.10028	2457938.85598	26.74	26.42	0.14	43.32	42.31	0.060	351.797	10.42
id8i23icq	2457939.10640	2457938.86210	26.97	26.65	0.14	43.32	42.31	0.060	351.797	10.64
id8i23ieq	2457939.11251	2457938.86821	27.10	26.78	0.14	43.32	42.31	0.060	351.797	10.78
id8i24igq	2457939.15428	2457938.90998	26.70	26.38	0.12	43.32	42.31	0.059	351.797	10.38
id8i24ihq	2457939.16039	2457938.91609	26.74	26.42	0.12	43.32	42.31	0.059	351.797	10.42
id8i24ijq	2457939.16650	2457938.92220	26.82	26.50	0.12	43.32	42.31	0.059	351.797	10.49
id8i24ilq	2457939.17261	2457938.92831	26.67	26.35	0.12	43.32	42.31	0.059	351.797	10.34
id8i24inq	2457939.17872	2457938.93442	26.98	26.66	0.12	43.32	42.31	0.059	351.797	10.65

through every possible period and folds the data, then fits a second-order Fourier series to each folded lightcurve (Buie et al., 2018a, 2018b); hereafter referred to as the "Fourier PDM" technique. This modeling is different from the traditional PDM which bins the data and looks for the place where the points in the bins are not as dispersed as other periods, but it has the advantage of being able to deal with data that are very sparsely sampled. For our dataset we searched a range of periods between 2 and 100 h (single-peaked; 4–200 h double-peaked) then focused on better-sampled periods between 2 and 30 (4–60) hours. We used a step interval of 1,000,000 which is dependent upon the search range, but at the lowest resolution samples periods every 30 s. We are suspicious of periods near to 3.2 h because these are commensurate with double the HST sampling rate (96 min), however we do not exclude them from our testing range.

As a check on our methodology, we also ran a Lomb-Scargle analysis (Scargle, 1982; Press and Rybicki, 1989) on our datasets to look for consistency between different period estimation techniques. This technique should work for the 9-day 2017 lightcurve campaign, but is not designed for the extremely sparse sampling of the astrometric dataset.

In the Fourier PDM the "goodness of fit" parameter is a chi-square measurement so the lower this value the better the fit. In the Lomb-Scargle model the "goodness of fit" parameter is measured as a peak in the periodogram so the higher the value the more likely the result. For the lightcurve campaign (looking from 2 to 10, 2–40 and 2–100 h; Fig. 5) using both search algorithms we see what appear to be best-fit values at a single-peaked period of 3.4 h, double-peaked period of 6.8 h, however compared to the range of the plot, the marginal significance compared to other possible values is low. The Lomb-Scargle actually gives a slight preference for a period of 7.4 (14.8 double-peaked) hours. For the Fourier PDM the chi-square range is 0.35 units and the difference between the minimum and the average is only 1-sigma from the scatter. In the Lomb-Scargle model the range is 4.8, but there are clearly other peaks with not dis-similar significances near 10.8, 40 and even 90 h. If we analyze each of the 6-orbit individual lightcurve campaign segments with either of these two models we get similarly inconclusive results.

For the astrometric dataset alone if we allow short periods we mostly find peaks slightly < 4 h (8 h) which should not be commensurate with the HST orbit period since these data are mostly single HST orbit datasets. If we exclude periods shorter than 4 h (based on an assumed break-up rotational speed barrier; Romanishin and Tegler, 1999) we still find the best fit period to be near the lower limit of the search range. If we combine the datasets we find a period of 3.38 h, double-peaked period of 6.76 h, although if we exclude periods < 4 h we find a period near 21.6 h (43.2 h; Fig. 6). Since there are more data points in the lightcurve campaign (both in number and relevant spacing for lightcurve phasing) than in the entire astrometric campaign, this

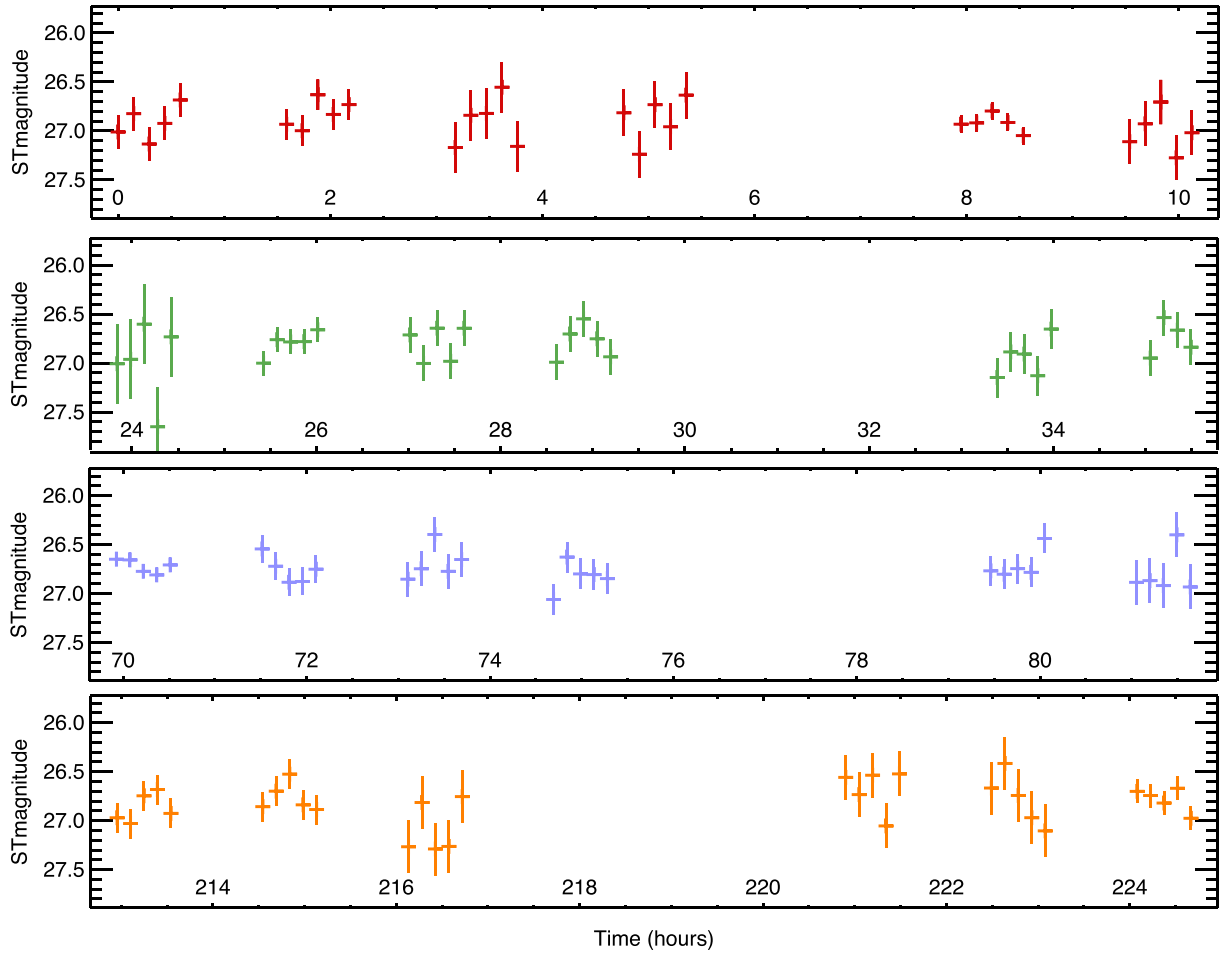

Fig. 3. Individual data points for each lightcurve campaign visit (sets of 6 semi-consecutive HST orbits) with 1-sigma error bars. The approximate 2-orbit gap between the measurements in each set was due to a telescope constraint that required HST to be repointed after no > 4 orbits. The gap does not severely impact the use of the data for our purposes.

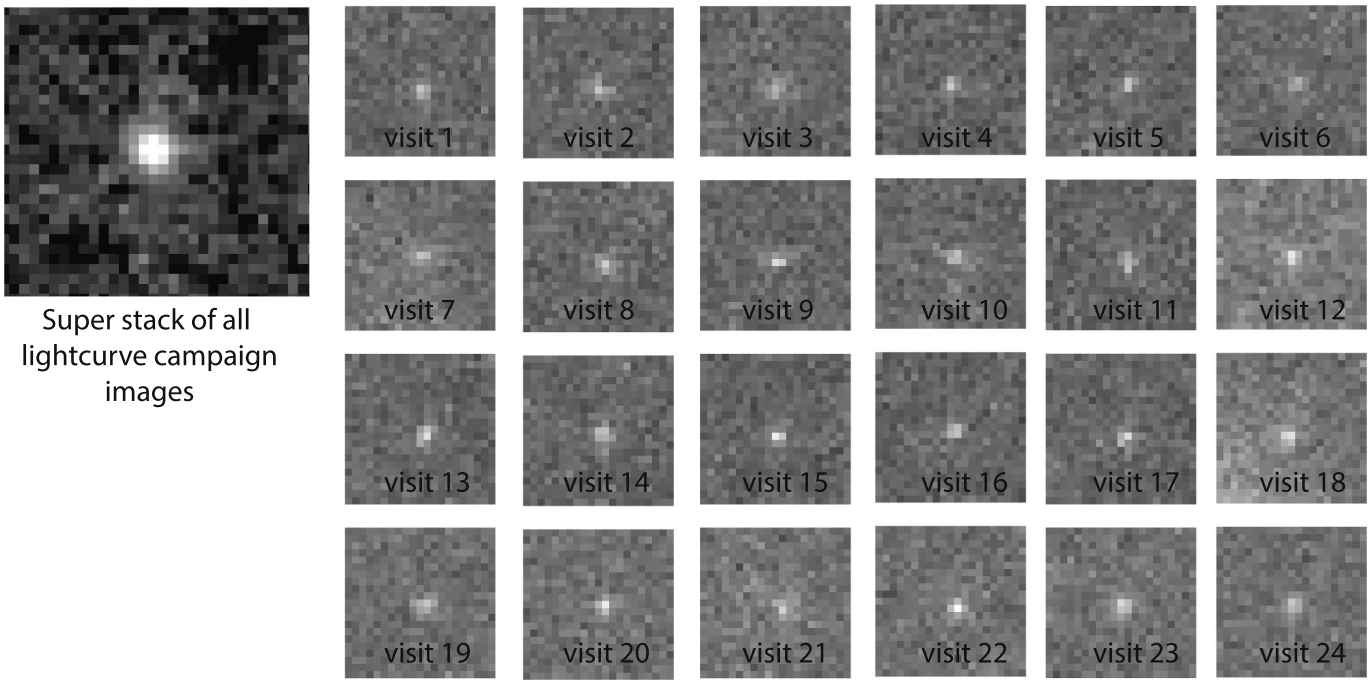

Fig. 4. HST image stacks for each lightcurve visit and from the entire lightcurve campaign. The magnitude limit is ~29.0 in the F350LP filter. There are no obvious satellites in these images and attempts at binary PSF fits confirm the lack of a binary detection at the resolution of HST.

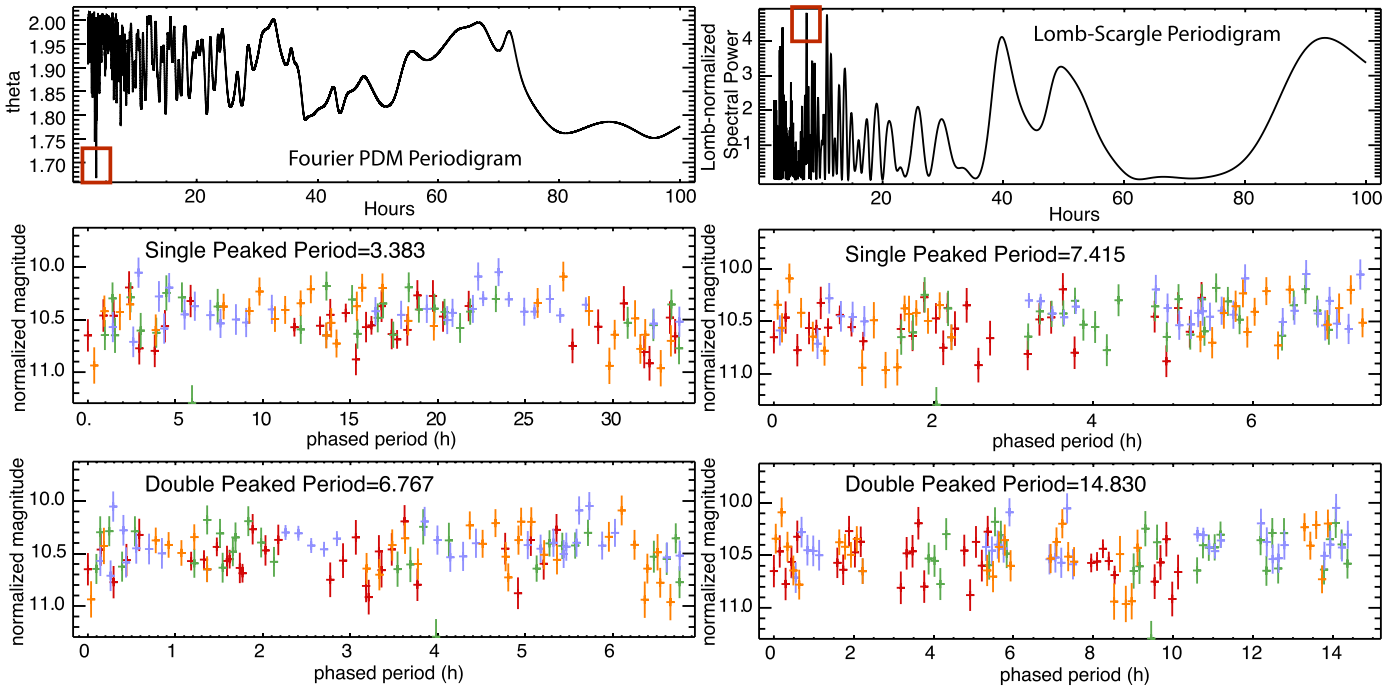

Fig. 5. (left) Fourier PDM Periodigram and (right) Lomb-Scargle Periodigram. The most consistent period derived from the lightcurve campaign (looking from 2 to 10, 2–40 and 2–100 h) using both search algorithms is a single-peaked period of 3.4 h, double-peaked period of 6.8 h. The Lomb-Scargle settles on a period of 7.4 (14.8 double-peaked) hours with a slightly stronger spectral power; however, in no case is one period found with statistical significance. The error bars (1-sigma in the plots) in both datasets are still quite large although the individual periods that come out of each individual analysis are somewhat consistent with each other.

lightcurve dataset still dominates the conclusion. We note that the astrometric campaign data does not appear to significantly contradict the results of the lightcurve campaign, however the chi-square range is still small compared to the best resultant chi-square. Therefore, we still believe there is too much uncertainty in the dataset to decisively settle on a best-fit period.

Finally, we use the data we have to place limits on the shape of MU69 and/or the geometry of the object by looking at the range of the data during each of the 6-orbit lightcurve segments, since this is the highest S/N dataset. The proposed variation, ≥ 0.3 magnitudes, that we used as a lower limit from the astrometric dataset alone in our original analysis is primarily due to the lower S/N of the photometry for measurements outside of opposition. When we fit solely to the lightcurve dataset we find that for any period the amplitude is between 0.15 and 0.5 magnitudes. Fits to the full 4-visit lightcurve dataset yield an amplitude of 0.15–0.2 magnitudes. Unfortunately, this is still comparable to the uncertainty in the dataset. While again this is not a definitive result, it does provide a useful physical limit and allows us to determine that MU69 is not significantly elongated (like the recently discovered interstellar visitor, Bannister et al., 2017; Meech et al., 2017) or suggests that the object orientation is approximately pointed in the observing direction; in either case there is no strong argument for adjusting the timing of the spacecraft encounter for observing a particularly long axis.

5.3. Elongation/shape

If MU69 is a triaxial ellipsoid with semi-major axes a ≥ b ≥ c in rotation about the c-axis, then the minimum and maximum flux of the rotation curve measured in magnitudes, Δm, can be used to determine the projection of the body shape (i.e. how spherical the object is) into the plane of the sky:

$$\Delta m = 2.5 \log \frac{a}{b} - 1.25 \log \left(\frac{a^2 \cos^2 \theta + c^2 \sin^2 \theta}{b^2 \cos^2 \theta + c^2 \sin^2 \theta} \right) \quad (2)$$

The parameter θ is the angle at which the rotation axis is inclined to the line of sight (an object with θ = 90° is being viewed equatorially; Binzel et al., 1989). If we make the extreme assumption that we are in fact viewing the object equatorially, then this equation can be rearranged to give the axis ratio, $a/b = 10^{0.4\Delta m}$, and in that case MU69 has an axis ratio of 1.15–1.2.

5.4. Synthetic modeling

5.4.1. HST dataset limits

Synthetic modeling provides another approach to understanding the limits of the HST dataset. We generate synthetic lightcurves for periods ranging from short (4 h) to long (100h) and with peak-to-peak amplitudes ranging from 0.2 to 0.6 magnitudes. We embed these lightcurves in the magnitude randomized HST dataset and then see how many of the synthetic lightcurves we can recover, and at what precision, using the same Fourier PDM analysis as described earlier. Fig. 7 gives the results for determining the amplitude of the real object in which we find unsurprisingly that the smaller the amplitude the more difficult it is to recover it accurately. This exercise demonstrates, since we do not measure an amplitude larger than ~0.15 magnitudes in the HST lightcurve campaign data, again, the strong suggestion that MU69 is NOT significantly elongated, or that its pole geometry is along the line of sight to Earth, or we are within the phase space for ambiguous interpretations/object configurations suggested by Harris et al. (2014).

5.4.2. Projected New Horizons optical navigation results

Using this same synthetic modeling, the timing and S/N of the *New Horizons* planned optical navigation (Op-Nav) and full body science images, the spacecraft data will allow us to determine the rotation period of MU69 during its 2018 approach and 2019 encounter. For a period of 5–10 h *New Horizons* should be able to resolve the period for an amplitude of 0.05 magnitudes or larger to within 0.01 h with 85% certainty. For a longer period of ~20 h *New Horizons* can resolve the same amplitude to within 0.1 h with the similar certainty. For a period

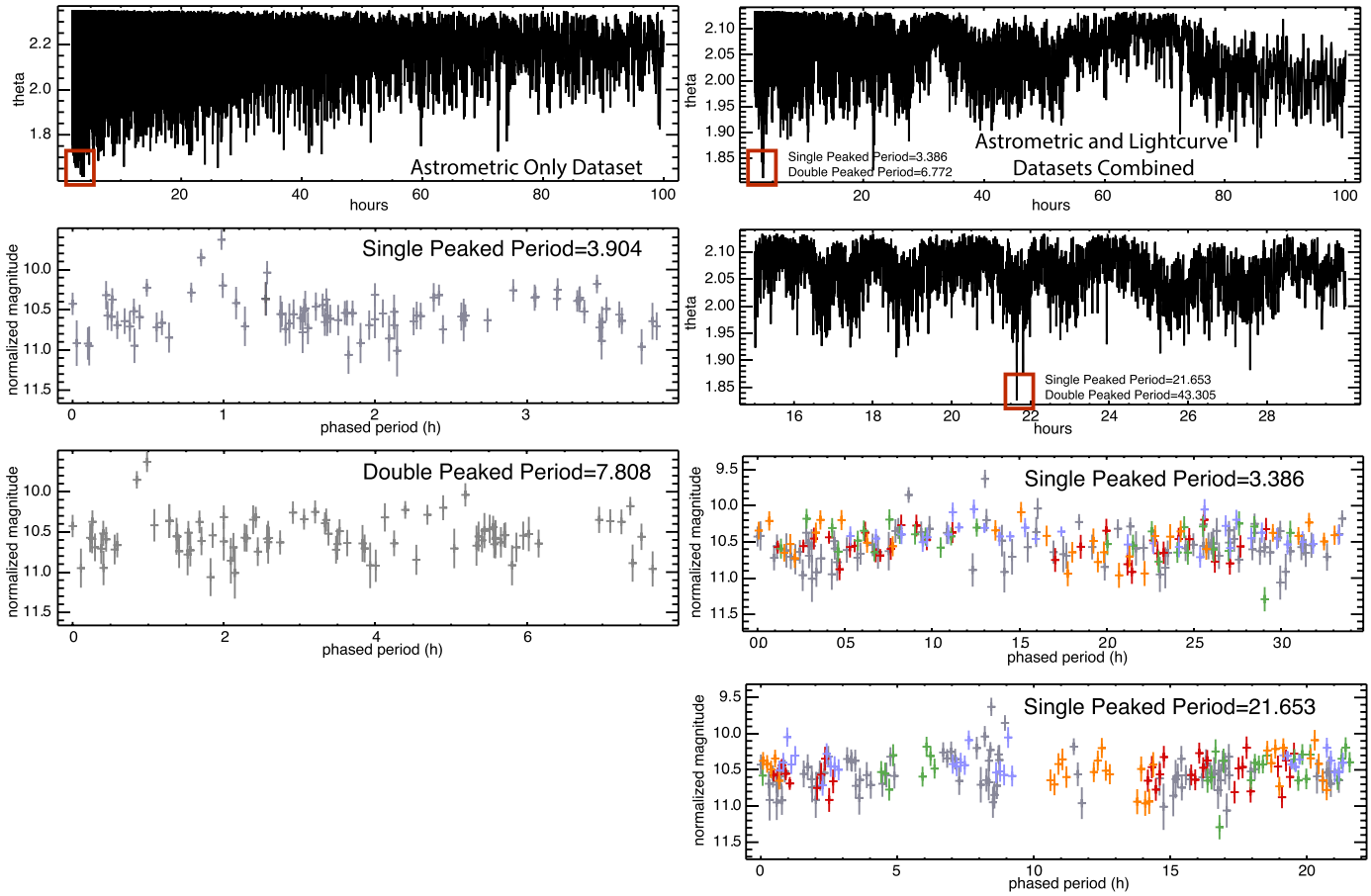

Fig. 6. (left) Astrometric-only dataset and (right) combined astrometric and lightcurve datasets using the Fourier PDM algorithm (with 1-sigma error bars). In the astrometric-only dataset, periods near the short end dominate the periodogram results. In the combined datasets we nearly exclusively find a period of 3.38 h, double-peaked period of 6.76 h, although if we exclude periods < 4 h we find a period near 21.6 h (43.2 h). Since there are more data points in the lightcurve campaign then in the entire astrometric campaign this first dataset still dominates the conclusion, but we note that the astrometric campaign data does not appear to contradict the short period interpretation. In any case our results are not statistically significant.

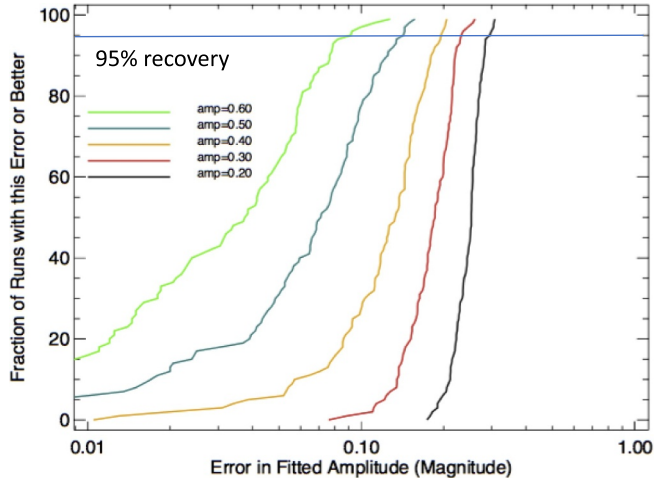

Fig. 7. Synthetic analysis of potential lightcurve amplitudes in which we seed the HST dataset with rotation curves having amplitudes ranging from 0.2 to 0.6 magnitudes with similar uncertainties as we have in the HST lightcurve campaign dataset. The larger the amplitude the easier it is to make an accurate determination. Fundamentally this tells us that if MU69 was rotating rapidly with a large amplitude, then we should have been able to detect that given the S/N in our data.

of ~40 h our accuracy drops to 50% and for a period of ~100 h it drops to 10%, however the period can still be determined to within a one hour uncertainty if it is low amplitude. If the amplitude is at least 0.15 magnitudes, the limit of the HST data, then *New Horizons* should be able to determine any period to an accuracy of better than 0.1 h in all cases and for periods less than ~20 h to an accuracy of better than 0.01 h. However, the in-situ images will allow for a clear rotational determination independent of the Op-Nav images since we can use surface features to unambiguously track MU69's rotational motion.

6. Summary and mission comparison

Despite the substantial amount of relatively high quality data acquired on MU69 using HST, we find that we cannot uniquely determine its rotation period and amplitude. The HST dataset presented here confirm with confidence that unless the pole vector is pointed close to the line of sight to Earth, MU69 is not rapidly rotating AND highly elongated (which we define as a lightcurve amplitude ≥ 0.5 magnitude). The data preclude the existence of a binary companion ≥ 2000 km with a sensitivity to 29th magnitude (an object a few km in size for assumed albedos of 0.04–0.15). Attempts to measure and model the lightcurve amplitude yield an average of 0.15 magnitudes, comparable to the scatter in the measurements themselves. An object with such a low amplitude lightcurve would be consistent with being relatively spherical, with an axis ratio < 1.15. One possible

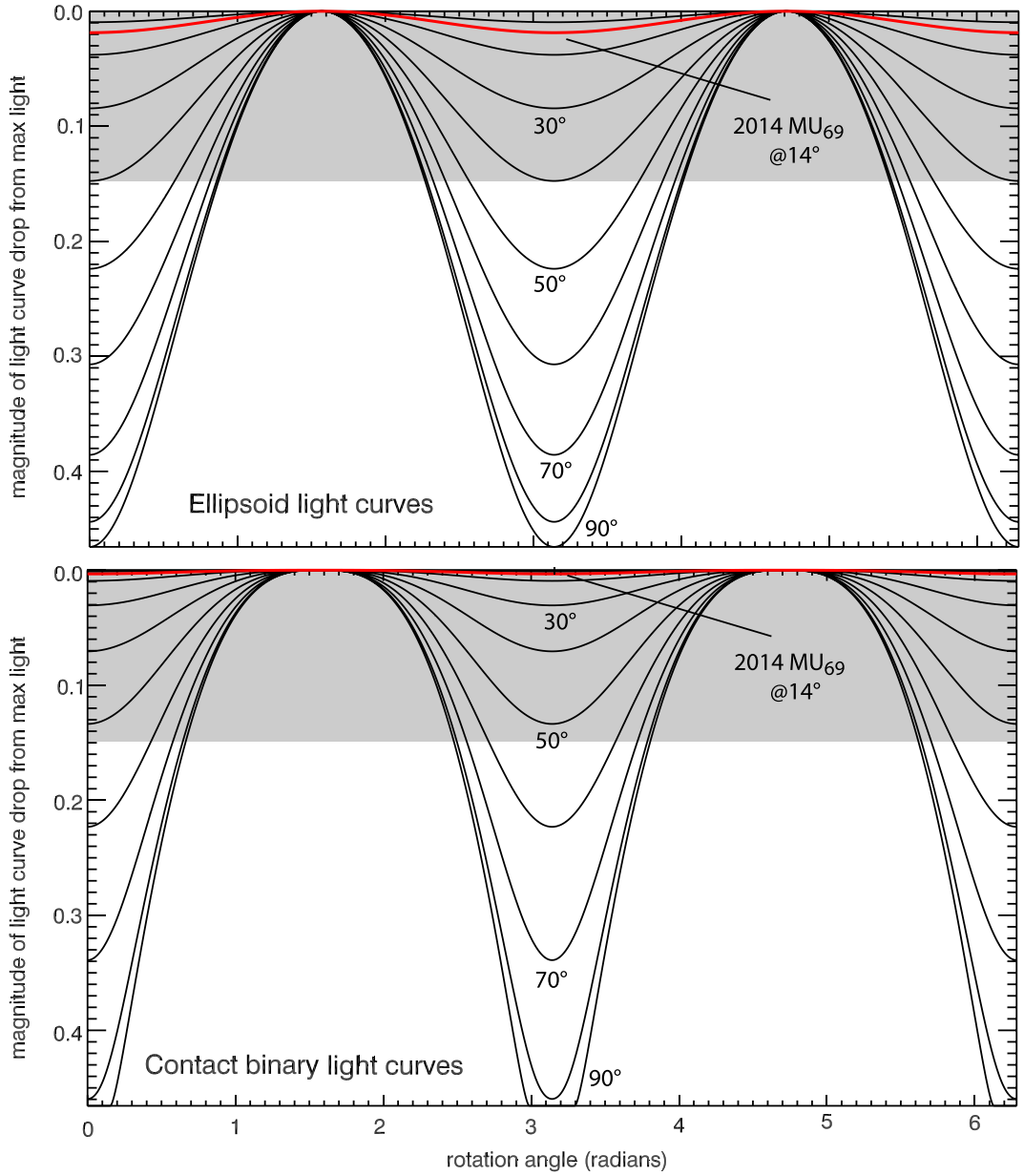

Fig. 8. (Top): Model ellipsoidal lightcurve results for the full range of pole inclinations based on the work of Connelly and Ostro, 1984. (Bottom) Model contact binary light curves for the full range of pole inclinations assuming both objects are completely spherical, there is no "neck" and that the light reflected from each object is exactly proportional to the visible object area. The 14° inclination of 2014 MU69's pole relative to the Earth is highlighted in red on each of these plots and changes by a factor of 6 between the two configurations. While these models are both simplistic, for a lightcurve amplitude as large as the scatter in our data, 0.15 magnitudes, to be produced would require a contact binary pole inclination of ≥52° or an ellipsoidal pole inclination of ≥40° (gray area in each plot). (For interpretation of the references to colour in this figure legend, the reader is referred to the web version of this article.)

explanation for a small lightcurve amplitude is that HST is viewing MU69 nearly pole-on or with the line of sight nearly perfectly pointed towards Earth. If this configuration is correct, then MU69 could still be significantly elongated and present a low amplitude variation. The lightcurve period and shape remains undetermined and does not rule out the possibility of a near-contact binary, or bi-lobed, interpretation proposed by stellar occultation data (Buie et al., 2018a, 2018b).

Finally, since this paper will come out after the MU69 encounter with *New Horizons* we reflect on our results in the context of the fly-by images (Stern et al., 2019, in press). Op-Nav data up to the point of encounter still produced a non-unique rotational period. The first resolved image of MU69 showed it to be a bi-lobed object consistent with the occultation results. The higher resolution images acquired during the fly-by showed that it is in fact rotating in a face-on/line of sight orientation such that the lobes rotate around a common center point, but the same overall surface-area is more or less always pointed towards Earth. In other words, the spin axis of MU69 lies within the cone within which the brightness variations due to a changing cross-section is smaller than the photometric errors in our measurements (Lacerda and Luu, 2003). This is one of the ambiguous results presented in Harris et al. (2014) and is consistent with our lightcurve non-detection.

The fact that the object is bi-lobed also significantly impacts the lightcurve amplitude that we observed in that a fully elliptical object rotating in the same way would present a lightcurve with a comparatively larger amplitude. Using the preliminary reported pole (Porter et al., 2019,) of J2000 RA = 300° and Dec −21°, we calculate that the Earth-pole angle viewing angle of MU69 was inclined to the viewer 14° (Zangari et al., 2019). Combining this information with preliminary

size measurements for the two lobes (9.73 ± 0.02 km and 7.12 ± 0.06 km, Stern et al., 2019, Bierson et al., 2019), we can estimate the approximate light curve amplitude we might have observed. Under the assumption that both objects are completely spherical, there is no "neck," and that the light reflected from each object is exactly proportional to the visible object area, Fig. 8 shows the lightcurve for several pole inclinations with the preliminary 14° estimate highlighted giving an idealized lightcurve amplitude of 0.003 magnitudes. For comparison, a projected ellipsoid model (Connelly and Ostro, 1984) with identical edge-on maxima and minima to the contact binary would have an amplitude of 0.019 magnitudes, a factor of 6 larger. Unfortunately, both of these values are well below the minimum detectable lightcurve amplitude of 0.15 magnitudes reported herein and even below any feasible photometry accuracy for an object of this magnitude from any ground-based or Earth-orbit facility. While these models are both simplistic, for a lightcurve amplitude as large as the scatter in our data, 0.15 magnitudes, to be produced would require a contact binary pole inclination of $\geq 52^{\circ}$ or an ellipsoidal pole inclination of $\geq 40^{\circ}$. This observation suggests that within the KBO lightcurve literature there are probably other objects which share a geometric configuration like MU69 resulting in an underestimate of the contact binary fraction for the Cold Classical Kuiper Belt.

Acknowledgments

Observations were made with the NASA/ESA Hubble Space Telescope, obtained at the Space Telescope Science Institute, which is operated by the Association of Universities for Research in Astronomy, Inc., under NASA contract NAS 5-26555. These observations are associated with programs GO-14627, GO-13663, GO-14485, GO-14629, and GO-15158. Support was provided by NASA through a grant from the Space Telescope Science Institute, which is operated by the Association of Universities for Research in Astronomy, Inc., under NASA contract NAS 5-26555. The modeling efforts in this work were supported by the National Aeronautics and Space Administration under Grant/Contract/Agreement No. NNX15AE04G issued through the SSO Planetary Astronomy Program. Some coauthors acknowledge support from the NASA *New Horizons* Project. We thank an anonymous reviewer for their helpful comments on this manuscript.

References

Bannister, M.T., et al., 2017. Col-OSSOS: colors of the interstellar Planetesimal 1I/'Oumuamua. Astrophys. J. 851, L38.

Benecchi, S.D., Sheppard, S.S., 2013. Light curves of 32 large transneptunian objects. Astron. J. 145 (5), 124. https://doi.org/10.1088/0004-6256/145/5/124.

Benecchi, S.D., Noll, K.S., Grundy, W.M., Buie, M.W., Stephens, D.C., Levison, H.F., 2009. The correlated colors of transneptunian binaries. Icarus 200, 292. https://doi.org/10.1016/j.icarus.2008.10.025.

Bierson, et al., 2019. LPSC 50.

Binzel, R.P., Farinella, P., Zappala, V., Cellino, A., 1989. In: Binzel, R.P., Gehrels, T., Matthews, M.S. (Eds.), Asteroids II; Proceedings of the Conference. Univ. of Arizona Press, Tucson, pp. 416–441.

Bowell, E., Hapke, B., Domingue, D., et al., 1989. In: Binzel, R.P., Gehrels, T., Matthews, M.S. (Eds.), Asteroids II. Univ. Arizona Press, Tucson, AZ, pp. 524–556.

Buie, M.W., Zangari, A.M., Marchi, S., Levison, H.F., Mottola, S., 2018a. Light Curves of Lucy Targets: Leucus and Polymele. 155. pp. 245. https://doi.org/10.3847/1538-3881/aabd81.

Buie, M., et al., 2018b. Pre-encounter update on (486958) 2014MU69 and occultation results from 2017 and 2018. In: AAS/Division for Planetary Sciences Meeting Abstracts 509.06.

Connelly, R., Ostro, S.J., 1984. Ellipsoids and lightcurves. In: NASA STI/Recon Technical Report A. 17. pp. 87.

Duffard, R., Ortiz, J.L., Thirouin, A., Santos-Sanz, P., Morales, N., 2009. Transneptunian Objects and Centaurs From Light Curves. https://doi.org/10.1051/0004-6361/200912601.

Harris, A.W., Pravec, P., Galád, A., Skiff, B.A., Warner, B.D., Világi, J., Gajdoš, Š., Carbognani, A., Hornoch, K., Kušnirák, P., Cooney, W.R., Gross, J., Terrell, D., Higgins, D., Bowell, E., Koehn, B.W., 2014. On the maximum amplitude of harmonics of an asteroid lightcurve. Icarus 235, 55.

Jewitt, D., Luu, J., 1993. Discovery of the candidate Kuiper belt object 1992 QB1. Nature (362), 730–732 (ISSN 0028-0836).

Krist, J., Hook, R., 2004. The Tiny Tim User's Guide: Version 6.3. STScI, Baltimore available at: http://www.stsci.edu/software/tinytim/.

Lacerda, P., Luu, J., 2003. On the detectability of lightcurves of Kuiper belt objects. Icarus 161, 174.

Meech, K.J., et al., 2017. A brief visit from a red and extremely elongated interstellar asteroid. Nature 552, 378.

Porter, S.B., Buie, M.W., Parker, A.H., Spencer, J.R., Benecchi, S., Tanga, P., Verbiscer, A., Kavelaars, J.J., Gwyn, S.D.J., Young, E.F., Weaver, H.A., Olkin, C.B., Parker, J.W., Stern, S.A., 2018. High-precision orbit fitting and uncertainty analysis of (486958) 2014 MU69. Astron. J. 156, 20.

Porter, et al., 2019. A Contact Binary in the Kuiper Belt: The Shape and Pole of (486958) 2014 MU_{69}. LPSC 50.

Press, W.H., Rybicki, G.B., 1989. Fast algorithm for spectral analysis of unevenly sampled data. Astrophys. J. 338, 277–280. https://doi.org/10.1086/167197.

Press, W.H., Teukolsky, S.A., Vetterling, W.T., Flannery, B.P., 1992. Numerical Recipes in C, second ed. Cambridge University Press, New York.

Rabinowitz, D.L., Barkume, K., Brown, M.E., Roe, H., Schwartz, M., Tourtellotte, S., Trujillo, C., 2006. Photometric observations constraining the size, shape, and albedo of 2003 EL61, a rapidly rotating, Pluto-sized object in the Kuiper Belt. Astrophys. J. 639, 1238.

Rajan, A., et al., 2011. "WFC3 Data Handbook", Version 2.1. STScI, Baltimore. http://www.stsci.edu/hst/wfc3/documents/handbooks/currentDHB/wfc3_dhb.pdf.

Romanishin, W., Tegler, S.C., 1999. Rotation rates of Kuiper-belt objects from their light curves. Nature 398, 129. https://doi.org/10.1038/18168.

Scargle, J.D., 1982. Studies in astronomical time series analysis. II - statistical aspects of spectral analysis of unevenly spaced data. Astrophys. J. 263, 835–853. https://doi.org/10.1086/160554.

Stellingwerf, R.F., 1978. Astrophys. J. 224, 953–960.

Stern, S.A., Weaver, H.A., Spencer, J.R., Elliot, H.A., the New Horizons Team, 2018. The New Horizons Kuiper Belt extended mission. Space Sci. Rev. 2018 (214), 77. https://doi.org/10.1007/s11214-018-0507-4.

Stern, S.A., et al., 2019. Overview of Initial Results From the Reconnaissance Flyby of a Kuiper Belt Planetesimal: 2014 MU_{69}. LPSC 50.

Thirouin, A., Sheppard, S.S., Noll, K.S., Moskovitz, N.A., Ortiz, J.L., Doressoundiram, A., 2016. Rotational properties of the Haumea family members and candidates: short-term variability. Astron. J. 151, 148.

Trilling, D.E., Bernstein, G.M., 2006. Light curves of 20–100 km Kuiper Belt objects using the Hubble space telescope. Astron. J. 131, 1149.

Walker, M.F., Hardie, R., 1955. A photometric determination of the rotational period of Pluto. Publ. Astron. Soc. Pac. 67, 224.

Zangari, et al., 2019. The Mysterious Missing Light Curve of (486958) 2014 MU_{69}, A Bilobate Contact Binary Visited by New Horizons. LPSC 50.